

Controlling Metal-Insulator Transitions in Vanadium Oxide Thin Films by Modifying Oxygen Stoichiometry

Min-Han Lee^{1,2,}, Yoav Kalcheim², Javier del Valle^{2,+}, and Ivan K. Schuller^{1,2}*

¹*Materials Science and Engineering Program, University of California San Diego, La Jolla, California 92093, USA*

²*Department of Physics and Center for Advanced Nanoscience, University of California San Diego, La Jolla, California 92093, USA*

⁺*Present address: Department of Quantum Matter Physics, University of Geneva, Quai Ernest-Ansermet 24, 1205 Geneva, Switzerland*

Abstract:

Vanadium oxides are strongly correlated materials which display metal-insulator transitions as well as various structural and magnetic properties that depend heavily on oxygen stoichiometry. Therefore, it is crucial to precisely control oxygen stoichiometry in these materials, especially in thin films. This work demonstrates a high-vacuum gas evolution technique which allows for the modification of oxygen concentration in VO_x thin films by carefully tuning thermodynamic conditions. We were able to control the evolution between VO₂, V₃O₅, and V₂O₃ phases on sapphire substrates, overcoming the narrow phase stability of adjacent Magnéli phases. A variety of annealing routes were found to achieve the desired phases and eventually to control the metal-insulator transition (MIT). The pronounced MIT of the transformed films along with the detailed structural investigations based on x-ray diffraction measurements and reciprocal space mapping show that optimal stoichiometry is obtained and stabilized. Using this technique, we find that the thin film V-O phase diagram differs from that of the bulk material due to strain and finite size effects. Our study demonstrates new pathways to strategically tune the oxygen stoichiometry in complex oxides and provides a roadmap for understanding the phase stability of VO_x thin films.

1. INTRODUCTION

Metal-insulator transitions (MITs) in oxides have been of special interest in condensed matter physics^[1-2] and technology^[3] in past decades. Specifically, vanadium oxides (VO_x) are considered very promising materials for next-generation oxide electronics. For instance, VO_2 has attracted much attention owing to its MIT near room temperature ($T_{\text{MIT}} \sim 340$ K), in which a large increase in electric resistivity is accompanied by a structural phase transition (SPT).^[4-5] Additional interest in VO_2 concerns the possibility of modulating this transition by external stimuli.^[6-8] The significant change in electrical resistivity offers a platform for resistive switching^[9] and neuromorphic computation^[10-12] related applications. In pure and Cr-doped V_2O_3 , the concurrence of metal-insulator, structural and magnetic phase transitions have been the subject of much fundamental research.^[13-16] The V_3O_5 phase, as one of the only two VO_x members with a MIT above room temperature ($T_{\text{MIT}} \sim 430$ K), is an excellent candidate for use in silicon-based technologies^[17] and switching device applications.^[18-20] During this MIT transition, the lattice structure remains monoclinic with a change in space group symmetry from $I2/c$ to $P2/c$. The possibility to trigger the MIT without a significant structural change is a great advantage for V_3O_5 based switching devices.

Vanadium oxides are very sensitive to changes in oxygen stoichiometry. Vanadium is a multivalent element displaying oxidation states between V^{2+} and V^{5+} , which gives rise to a series of compounds known as Magnéli ($\text{V}_n\text{O}_{2n-1}$) and Wadsley phases ($\text{V}_n\text{O}_{2n+1}$).^[21-23] The existence of multiple phases leads to a complicated V-O phase diagram.^[24-26] Furthermore, shrinking them into thin films or other nanoscale structures is needed to increase their functionality.^[27] Typically, the V-O phase diagram is constructed with the thermodynamic data of bulk samples. However, as the size is reduced, the increase in the surface-to-volume ratio introduces an additional surface energy term in the Gibbs free energy that might affect the thermodynamically stable phase region.^[28-29] Despite decades of research, a comprehensive understanding of thin film thermodynamics in the VO_x system is still lacking. Most studies have only focused on the growth of VO_2 thin films and the improvement of their MIT properties by thermal annealing.^[2,3,30-32] Other oxides such as V_3O_5 , which is the closest Magnéli phase to V_2O_3 , is particularly difficult to deposit directly because of the narrow range of allowable oxygen stoichiometry (with an O/V ratio between 1.666 and 1.668 ± 0.002).^[33-34] The fabrication of V_3O_5 film in a recent work still contains small amount of V_2O_3 impurities.^[35] In general, obtaining high quality thin films of a specific VO_x and understanding the thin film phase diagram remains a challenging task.

In this study, we achieved control over oxygen stoichiometry in vanadium oxide thin films by using a high-vacuum gas evolution system. The experimental setup is shown in Fig. 1a. (see the experimental section for more details) We first sputtered VO_2 or V_2O_3 thin films on sapphire ($\alpha\text{-Al}_2\text{O}_3$) substrates and then placed the samples in the center of a high vacuum tube furnace for heat treatment using ultra high purity oxygen. A similar technique has been used to control oxygen deficiency in high-temperature superconducting $\text{YBa}_2\text{Cu}_3\text{O}_{7-x}$ samples.^[36-37] Starting from single-phase VO_2 or V_2O_3 films, we are able to transform the initial material into a different VO_x film by carefully following a controlled route in the partial oxygen pressure (PO_2)-temperature (T) diagram. (Fig. 1b.) Various routes were tested

to optimize the purity and enhance the MIT properties of the resulting compound. After treatment, the resulting phases were investigated using x-ray diffraction (XRD), reciprocal space mapping (RSM) and transport measurements. We show that our technique can provide excellent control over a wide-range of temperatures and oxygen partial pressures down to high vacuum conditions, allowing us to minimize the effect of other gases or contaminations. This offers significant advantages over normal thermal oxidation/reduction methods using gas mixture with limited vacuum range (≥ 0.01 torr).^[38] The precision of our method is shown by obtaining single-phase V_3O_5 thin films with the pronounced MIT despite their extremely narrow phase stability range. We are thus able to modulate the metal-insulator transitions between different phases and construct a detailed vanadium-oxygen phase diagram for thin VO_x films.

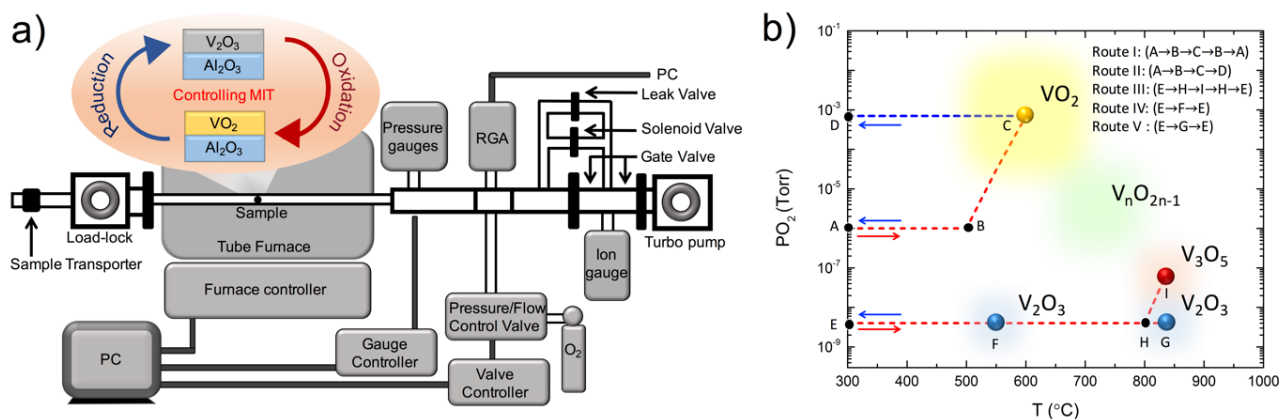


FIG. 1. (a) Schematic illustration of the gas evolution setup used to control the oxygen stoichiometry in VO_x . (b) Synthesis pathways in the thermodynamic phase diagram of VO_x thin films. The dashed lines represent the different heating/cooling routes for preparing various phases of vanadium oxide.

2. RESULTS AND DISCUSSION

2.1 Evolution of V_2O_3 phase into VO_2

Figure 2a shows electrical transport of V_2O_3/Al_2O_3 (r-cut) thin films before and after different gas evolution treatments. The R-T curve of as-deposited V_2O_3 shows a sharp metal-insulator transition (MIT) at $T_{MIT} \sim 160$ K, with at least a six orders of magnitude change in electrical resistance and a 10 K thermal hysteresis between the heating and cooling branches. The single-phase growth of V_2O_3 thin film on r-cut sapphire is confirmed by the XRD scan shown in Fig 2b. The scattering intensity of the V_2O_3 is much stronger than sapphire when we align the x-ray to the V_2O_3 peak. There are three out-of-plane diffraction peaks corresponding to (012), (024) and (036) corundum V_2O_3 phase. X-ray measurements on similar films^[39] suggest that the V_2O_3 grows epitaxially along the crystallographic orientation of the (012) sapphire substrate orientation. By following the annealing process (route I) in the PO_2 -T phase diagram (Fig. 1b), this film was transformed into VO_2 , with a three orders of magnitude MIT at $T_{MIT} \sim 340$ K (Fig. 2a). Interestingly, this MIT was significantly improved and enhanced by following route II. The resulting VO_2 phase was confirmed by reciprocal

space mapping (RSM) (see Fig. 2f and 2g). The absence of diffraction peaks from other Magnéli phases indicates the formation of single-phase VO₂ films.

Figure 2b shows the XRD spectra for (route I)-annealed and (route II)-annealed samples. XRD patterns for samples subjected to both routes, clearly show the diffraction peak at 37.1°, corresponding to the (200) plane of the VO₂ monoclinic structure. The resulting VO₂ films still exhibit preferred orientation with the (200) plane pointing at ~40° to the surface normal ($\chi \sim 40^\circ$), while for the directly sputtered VO₂ films on r-cut sapphire, the (200) plane is parallel to the substrate surface ($\chi \sim 0^\circ$) (Fig. 4b). The formation of a tilted (200) plane indicate the lack of well-aligned epitaxial layers and the appearance of disorder at the VO₂/Al₂O₃ interface, as present in many oxide heterostructures.^[40] It should be noted that there are structural similarities between rutile VO₂ and corundum V₂O₃. Previous studies have shown that through a common parent structure with hexagonal-close-packing arrangement, VO₂ and V₂O₃ may be derived from each other through a well-defined symmetry-breaking mechanism along the [001] direction of corundum V₂O₃ and the [100] of rutile VO₂.^[41] It is thus unlikely that formation of VO₂ from V₂O₃ would be randomly oriented.

The AFM images demonstrate differences in surface morphology and roughness between the as-deposited V₂O₃ (Fig. 2c), (route I)-annealed film (Fig. 2d) and (route II)-annealed film (Fig. 2e). The root-mean-square (RMS) roughness extracted from the Fig. 2c, 2d and 2e was 5.62 nm, 6.22 nm and 8.29 nm, respectively. The original V₂O₃ film prepared by sputtering reveals a relatively smooth surface. The quenching process along route I results in a bigger grain size (~190 nm assuming spherical shape) of the VO₂ film. It is this (route I)-annealed VO₂ film which exhibits a smaller width in the hysteresis loop appearing in the R-T curve at the MIT (Fig. 2a). Consequently, our results suggest that the hysteresis loop at the MIT broadens with decreasing the grain size.^[42-43] Earlier reports show that smaller grains lead to a high density of grain boundaries resulting in a decrease in the magnitude of the resistivity change across the MIT.^[44] Alternatively, the larger resistance switching ratios and smaller grains (~75 nm) observed in (route II)-annealed VO₂ film, suggest that the change in electrical resistance cannot be solely due to a grain size effect. Oxygen stoichiometry must also play a role in the MIT behavior of VO₂. The activation energy (E_a) of VO₂ insulating state ($T \leq 310$ K) can be estimated from the linear fitting of the ratio $\ln R(T)/(1/k_b T)$, as $R(T) = R_0 \exp(E_a/k_b T)$. The results obtained from (route I)-annealed and (route II)-annealed VO₂ are ~191 meV and ~259 meV, respectively. Quenching the (route I)-annealed VO₂ film under relatively low PO₂ is likely to increase the density of defects and promote oxygen loss. These vacancies might have the effect of doping in the VO₂, thereby increasing the number of free charge carriers and reducing the magnitude of the resistive change across the MIT.^[45,46] Detailed phase stability diagram (Fig. 6.) also shows that annealing the sample in point C at 600 °C with low oxygen pressure will result in oxygen-deficient VO_{2-x} phases.

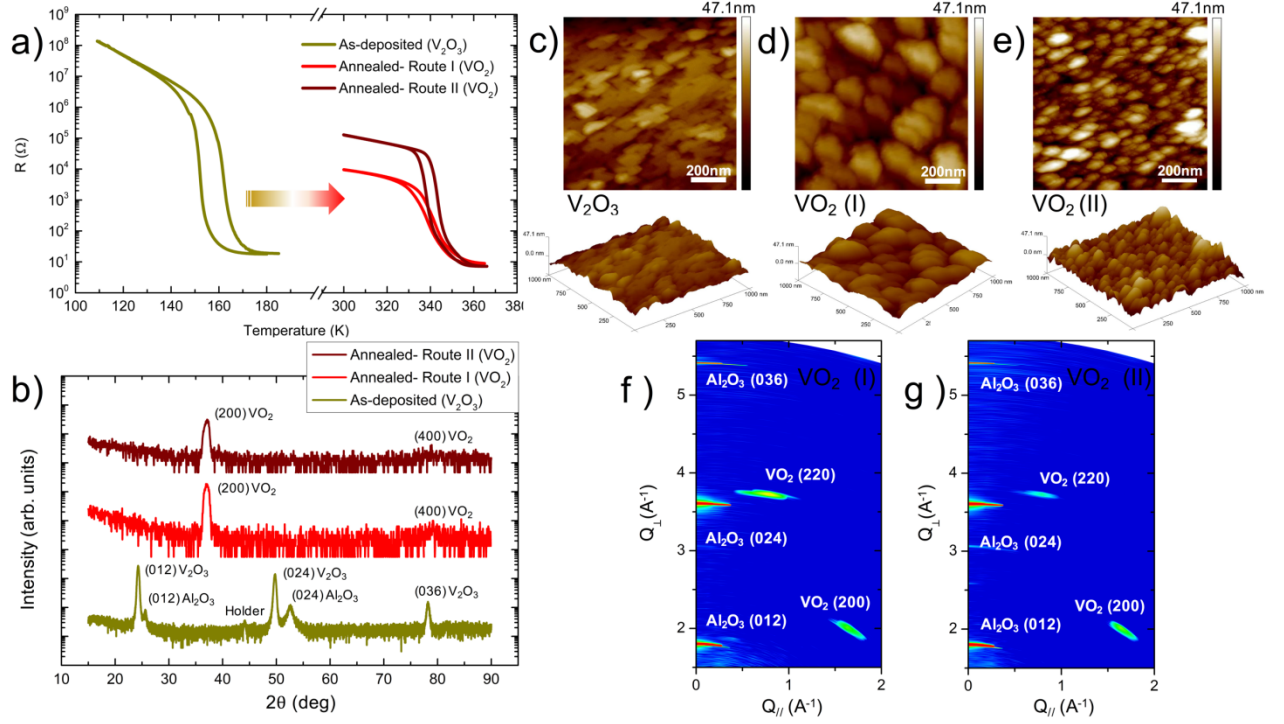


FIG. 2. Formation of VO_2 phase from V_2O_3 thin film on (012) *r*-cut sapphire substrate. (a) Resistance vs. temperature of vanadium oxide thin films under various oxidation conditions. After annealing, the thin films showed a sharp VO_2 metal-insulator transition at ~ 340 K. (b) Room-temperature XRD scans for vanadium oxide films. The different diffraction spectra correspond to the V_2O_3 phase (as-deposited) and the VO_2 phase (annealed following route I or route II). The crystallographic orientation of the VO_2 film was (200), which points along $\sim 40^\circ$ to the surface normal ($\chi \sim 40^\circ$). Angle (χ) denotes the degree between surface normal and the diffraction plane. AFM images ($1 \times 1 \mu\text{m}^2$) showing the surface morphology of (c) as-deposited film, (d) (route I)-annealed film and (e) (route II)-annealed film. The scale bar is 200 nm for all images. Reciprocal space mapping (RSM) of (f) (route I)-annealed and (g) (route II)-annealed VO_2 films. Q_{\perp} denotes the out-of-plane orientation (012) of Al_2O_3 .

2.2 Evolution of V_2O_3 phase into V_3O_5

Due to the numerous possible oxidation states, vanadium oxides are very sensitive to changes in oxygen content. Here, we show that oxidation of V_2O_3 to form the V_3O_5 can be achieved on *c*-cut and *r*-cut sapphire by slightly increasing the PO_2 at ~ 840 °C. Figure 3a displays the temperature dependent electrical transport of a V_2O_3 film grown on *c*-cut sapphire before and after the gas evolution treatment. The *R*-*T* curve of the as-deposited V_2O_3 film shows a suppressed metal-insulator transition with only a slight resistance variation. We note that this V_2O_3 sample was grown under the same conditions as the one shown in Fig. 2a, which shows a much more pronounced MIT. This suppression of the MIT in V_2O_3 grown on *c*-cut sapphire had been previously attributed to strain and microstructural effects between thin film and substrate.^[47,48] The lattice parameters and the *c/a* ratio of our epitaxial *c*-cut V_2O_3 thin film are ~ 2.81 ($a=b= 4.98$ Å; $c=14.01$ Å). This ratio is consistent with the reported value of *c*-cut V_2O_3 with unusual metal-insulator-metal behavior.^[47] In previous work, we have shown that

the structural phase transition and metal-insulator transition were robustly coupled to each other.^[16] Therefore, it is likely that the structural phase transition in our V_2O_3 sample is highly dependent on the a- and c-axis deformation as well. And this leads to the suppression of the MIT. The XRD pattern in Fig. 3b shows that corundum V_2O_3 film is highly oriented with the (001) c-cut sapphire substrate. By annealing this film along route III (Fig. 1b), we were able to transform it into a single-phase V_3O_5 film with an MIT of more than one order of magnitude at $T_{MIT} \sim 417$ K. The smooth MIT behavior above room temperature together with the absence of thermal hysteresis in the $R(T)$ are signs of a second-order phase transition, as reported previously.^[18,49]

The presence of a single-phase polycrystalline structure is confirmed by RSM as shown in Fig. 3e. The axis Q_{\perp} points along the out-of-plane orientation (001) for the Al_2O_3 substrate. Figure 3b shows six diffraction peaks at $2\theta = 36.0^\circ, 38.5^\circ, 38.9^\circ, 76.2^\circ, 82.3^\circ$ and 83.4° corresponding to the (020), (202), (400), (040), (404), and (800) planes in V_3O_5 , respectively.^[50] The AFM image of the as-deposited V_2O_3 film (Fig. 3c) indicates a relatively smooth film surface with 0.72 nm RMS roughness. The resulting V_3O_5 film shown in Fig. 3d has a much rougher surface with 13.1 nm RMS roughness. Furthermore, the grain structure is highly irregular after the treatment, as suggested by the XRD and RSM data.

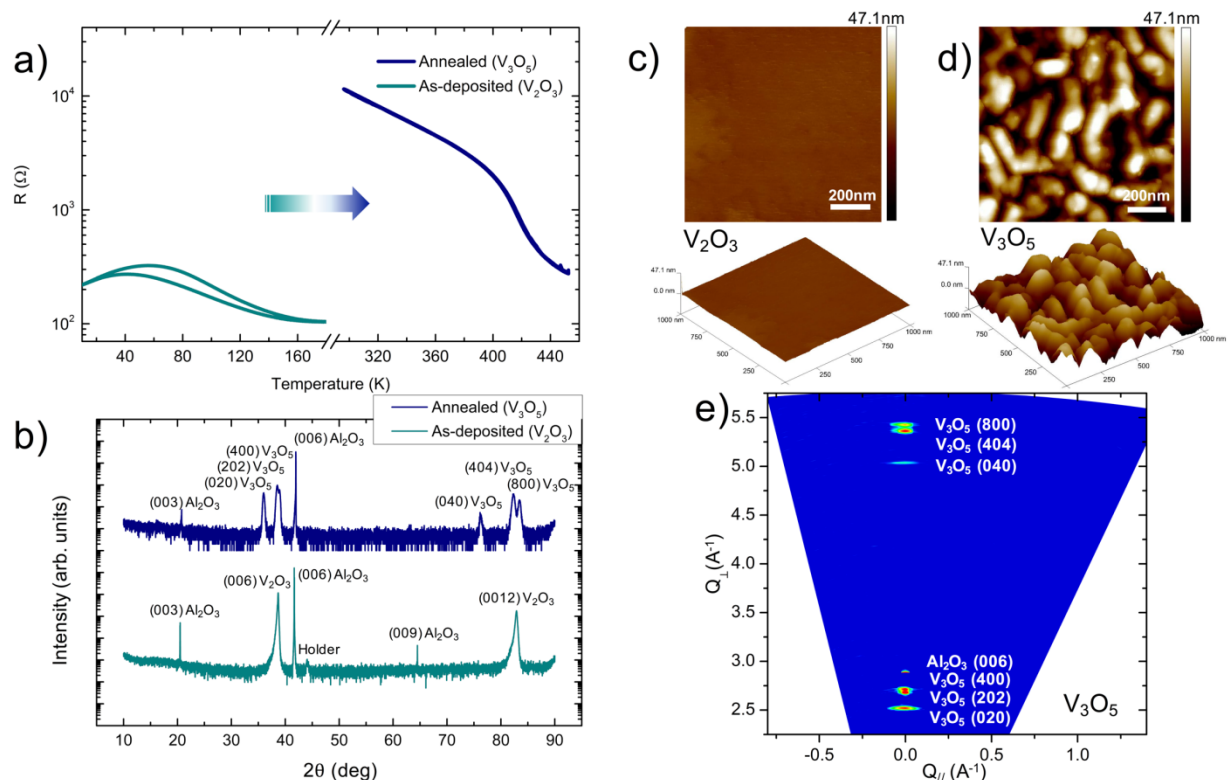


FIG. 3. Formation of V_3O_5 phase from V_2O_3 thin film on (001) c-cut sapphire substrate. (a) Resistance as a function of temperature of V_2O_3 film and resulting V_3O_5 film. The MIT temperature (T_{MIT}) of the V_3O_5 is ~ 417 K. (b) Room-temperature XRD scans. Evolution of different peaks corresponding to V_2O_3 phase (as-deposited) and V_3O_5 phase (annealed following route III). Preferred crystallographic orientations of V_3O_5 film were (020), (202) and (400). AFM images revealed the surface morphology of (c) as-deposited film and (d)

(route III)-annealed film. (e) X-ray RSM of the resulting V_3O_5 film. Q_{\perp} denotes the out-of-plane orientation (001) of Al_2O_3 (perpendicular to the film surface).

Figure 4a demonstrates the electrical transport of a V_2O_3 film on r-cut sapphire before and after gas evolution treatments along route III. After annealing at point I for 3 hours we observe an increase in resistance in the metallic states and a reduction of the magnitude of the hysteresis. However, the large MIT at $T_{MIT} \sim 150$ K indicates that the major phase in the film is still V_2O_3 . The formation of pure V_3O_5 phase is achieved by a second annealing process for an additional 6 hours along route III. The $R(T)$ starts showing a smooth MIT above room temperature ($T_{MIT} \sim 404$ K) without thermal hysteresis. Comparison of R-T curves of V_3O_5 films grown on c-cut (001) and r-cut (012) Al_2O_3 substrates is shown in Fig. 4b. Both samples reveal an MIT of more than one order of magnitude. For ease of comparison, the results were normalized by the metallic state resistance (R_{450K}). Since the transformed V_3O_5 films were polycrystalline, it is likely that the strain in the different grains is highly inhomogeneous. Different sapphire substrates will generate different dislocations and strain. Due to the numerous grain orientations, it is quite challenging to precisely quantify the strain in the polycrystalline thin film. By comparing the lattice spacings in V_3O_5 grown on r-cut and c-cut oriented sapphire, the structural distortion can still be estimated. Compared to the c-cut V_3O_5 thin film, the relative strains for the (100), (010), (001) planes of V_3O_5 /r-cut sapphire are considerably more compressed ($\Delta d_{100} \sim -0.71\%$; $\Delta d_{010} \sim -0.03\%$; $\Delta d_{001} \sim -2.1\%$). It is likely that larger compressive strain leads to lower T_{MIT} as found in a previous study which has shown that T_{MIT} in V_3O_5 decreases with pressure.^[51] The strain generated from the sapphire substrates and the difference in microstructure and grains might lead to the 14 K variation in T_{MIT} . Figure 4c shows the evolution of the crystalline structure for the V_2O_3 film. After 3 hours annealing, the intensity of the diffraction peaks decreased, but the thin film still remained corundum V_2O_3 . On the other hand, the second, lengthier annealing time (6 hours) allowed for a complete transformation into V_3O_5 . Besides the out-of-plane sapphire peaks, one diffraction peak from the V_3O_5 (310) plane was found at $\chi \sim 17^\circ$ (Fig. 4c and 4e). And several in-plane V_3O_5 peaks can be found using reciprocal space mapping. The RMS roughness of the transformed V_3O_5 film is 5.8 nm (Fig. 4d), close to the value of original sputtered V_2O_3 on r-cut sapphire (RMS roughness ~ 5.62 nm).

Interestingly, a large difference in the annealing times required to form V_3O_5 is observed for the two different substrates (012) and (001) Al_2O_3 . This indicates the crystallographic orientation of the film significantly affects thermodynamic kinetics and oxygen diffusion processes. As we observe from our x-ray diffraction measurements (Fig. 3b and 4c), for both substrates, in the final stage the samples only showed diffraction peaks associated with V_3O_5 (aside from the sapphire peaks) indicating high phase purity.

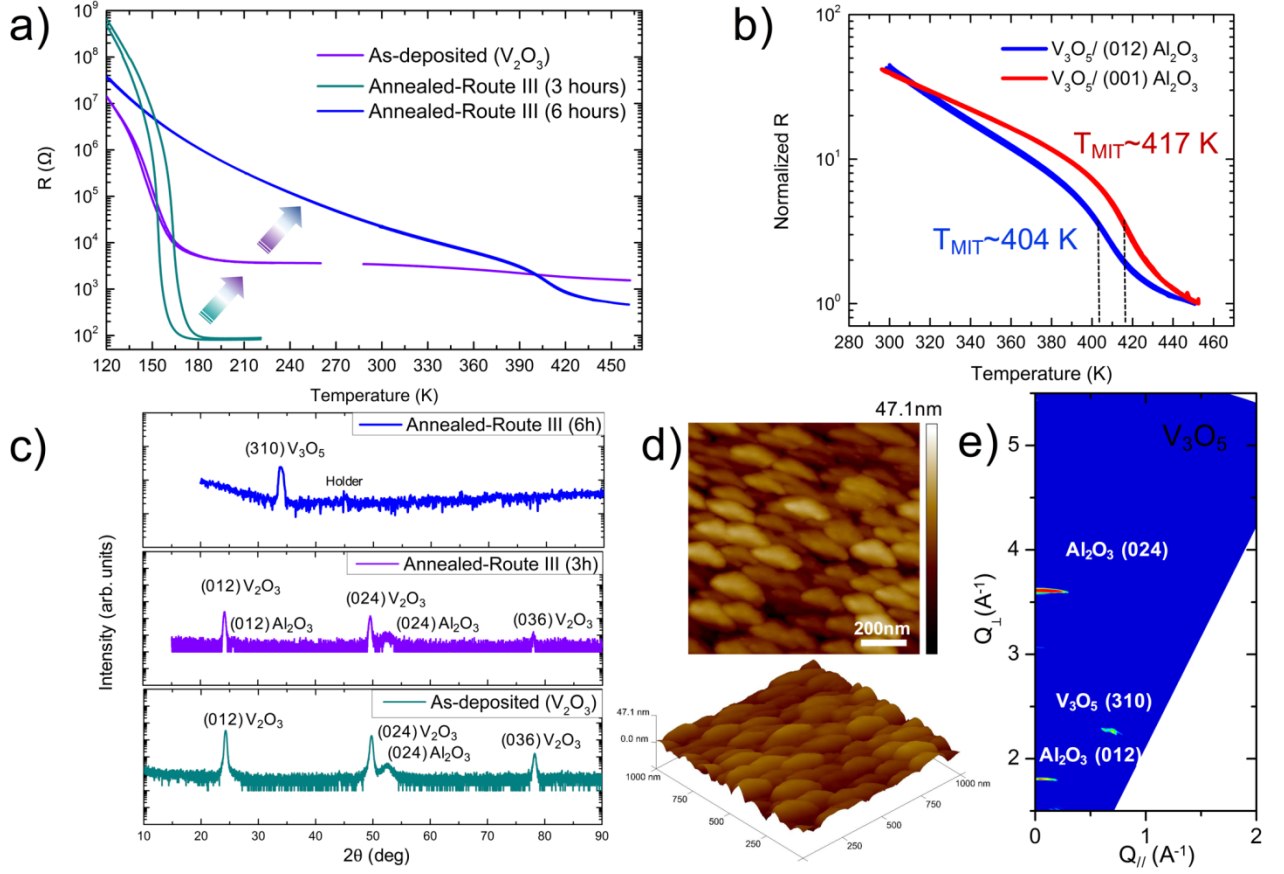


FIG. 4. Formation of V_3O_5 Phase from V_2O_3 thin film on (012) r-cut sapphire substrate. (a) Resistance as a function of temperature for a V_2O_3 film: as deposited film (cyan); after annealing for 3 hours at point I (purple); after annealing for additional 6 hours at point I (blue). (b) Comparison of the normalized $R(T)$ for V_3O_5 films on r-cut sapphire (blue) and c-cut sapphire (red). The black dashed lines mark the T_{MIT} for the two different samples. (c) XRD measurements of samples after time annealed V_2O_3 thin film following route III. Preferred crystallographic orientation of the resulting V_3O_5 film was (310), which point along $\sim 17^\circ$ to the surface normal ($\chi \sim 17^\circ$). (d) AFM images revealed the surface morphology (e) X-ray RSM of the resulting V_3O_5 film. Q_\perp denotes the out-of-plane orientation (012) of Al_2O_3 (perpendicular to the film surface).

2.3 Evolution of VO_2 phase into V_2O_3

In addition to the controlled oxidation of as-grown V_2O_3 thin films, we have also demonstrated and studied the controlled reduction of as-grown VO_2 thin films on r-cut sapphire. Figure 5a shows the electrical transport of a VO_2 film on an r-cut sapphire both before and after the gas evolution treatments along route IV. The R-T curve of as-deposited VO_2 shows a sharp metal-insulator transition (MIT) at $T_{MIT} \sim 340$ K, with more than a three orders of magnitude resistance change. The single-phase growth of VO_2 is confirmed by the XRD scan shown in Fig. 5b. Two reflection peaks corresponding to the (200) and (400) planes for monoclinic VO_2 are observed at $2\theta = 37.1^\circ$ and 79.0° , respectively. By following

the annealing process (route IV) shown in Fig. 1b, the highly textured VO₂ film was transformed into single-phase V₂O₃, now with a five orders of magnitude MIT with T_{MIT}~145 K. (see Fig. 5a) This value of the transition temperature T_{MIT} ~145K, is slightly lower than the value of the transition temperature T_{MIT} ~160K, for the directly sputtered V₂O₃ film, indicating that there might be a comparatively higher oxygen concentration in the transformed V₂O₃ film.^[52] Moreover, we find no significant differences ($\Delta 2\theta \leq 0.035^\circ$) in the out-of-plane (012) and in-plane (104) XRD peaks between directly sputtered V₂O₃ and transformed V₂O₃ films, ruling out strain effects as a major cause for the decrease in T_{MIT}. Previous studies on V₂O_{3+x} have shown that a 15K variation in T_{MIT} corresponds to an excess of oxygen concentration (x) of less than with 0.013.^[53,54] This provides an estimate of the accuracy of our control over oxygen content in a gas evolution process. The presence of an epitaxial V₂O₃ film was confirmed by XRD (Fig. 5b) and RSM scans (Fig. 5e). Both in-plane and out-of-plane crystallographic orientations in V₂O₃ follow the substrate orientations. This indicates that the structural similarity between corundum V₂O₃ and Al₂O₃ promotes epitaxial growth during the atomic rearrangement. Therefore, it is reasonable to conclude that the coupling to the Al₂O₃ substrate plays an important role in determining the crystallographic orientations of the transformed film. We note that this is in contrast to the case of VO₂ derived from a V₂O₃ film, which develops a different orientation after gas evolution compared to the as-grown VO₂ film. This may be due to the higher degree of compatibility between the Al₂O₃ substrate and the isostructural V₂O₃ compared to the rutile VO₂.

For the transformation of as-grown VO₂ films into single-phase V₂O₃, it takes 12 hours (point F in the PO₂-T diagram shown in Fig. 1b) to reach an equilibrium state. We found that the as-grown VO₂ films that were subjected to a shortened annealing process of only three or six hours along route IV did not exhibit any clear MIT behavior and no XRD peaks can be found. This suggests that thermodynamic equilibrium may not have been reached in this shorter period of time. However, the reverse transformation of as-grown V₂O₃ films into single-phase VO₂ films requires a shorter annealing time of three hours. The discrepancy between these two cases suggests that the phase evolution mechanisms are also associated with kinetics and diffusion processes which are beyond the scope of this work. Furthermore, the monoclinic VO₂ film could also be transformed into corundum V₂O₃ phase by following an alternate annealing treatment along route V. This indicates that point G in Fig. 1b is still in the V₂O₃ stable region. Figures 5c and 5d show the surface morphology of the as-deposited film and (route IV)-annealed film, respectively. The VO₂ film prepared by sputtering shows a textured surface with the RMS roughness equal to 5.98 nm. The resulting V₂O₃ after the loss of oxygen shows a relatively rougher surface with roughness up to 8.35 nm.

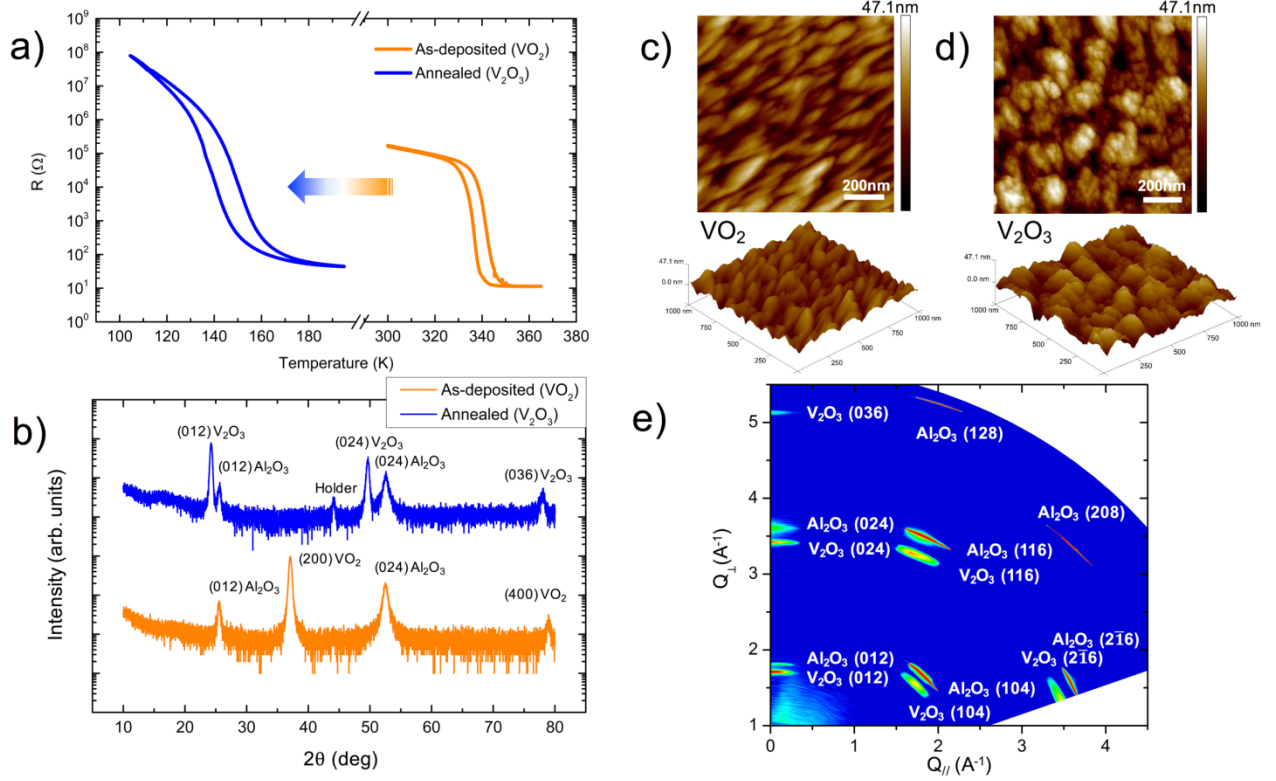


FIG. 5. Formation of V_2O_3 Phase from VO_2 thin film on (012) *r*-cut sapphire substrate. (a) Resistance as a function of temperature of VO_2 film and resulting V_2O_3 film. (b) Room-temperature XRD scans. Evolution of different peaks corresponding to VO_2 phase (as-deposited) and V_2O_3 phase (following annealing route IV). AFM images revealed the surface morphology of (c) as-deposited film and (d) annealed film. (e) Wide-range RSM of the transformed V_2O_3 film. Both in-plane and out-of-plane crystallographic orientations of the V_2O_3 film strongly followed the *r*-cut sapphire substrate orientations, suggesting the formation of epitaxial structures after gas evolution. Q_{\perp} denotes the out-of-plane orientation (012) of Al_2O_3 .

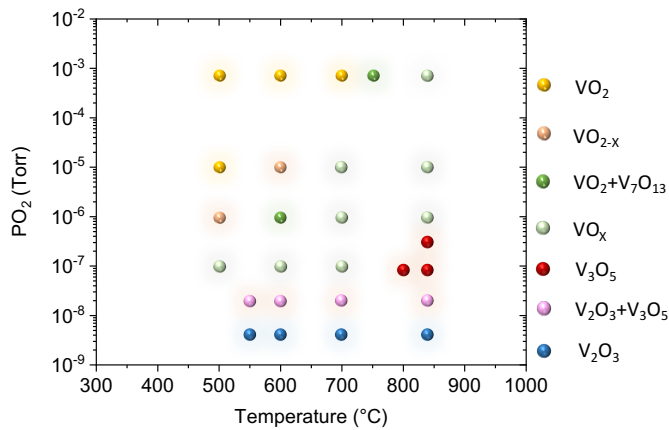


FIG. 6. *V-O* phase diagram for thin film. Circles represent the tested annealing condition.

Our technique can provide excellent control over a wide-range of temperatures and oxygen partial pressures, allowing us to explore a more complete picture of thin film phase diagram. It is worth noting that the V-O phase diagram (Fig. 6) we obtain starting from 100 nm V_2O_3 is substantially different from the bulk V-O phase diagram.^[24-26] Among all the Magnéli phases, the only thin film we could obtain in pure form was V_3O_5 and the annealing parameter range was very narrow. Moreover, starting from 10 nm thin films, despite tens of trials, we could not obtain V_3O_5 under the same annealing conditions. These condition differences as compared to the bulk phase diagram may be due to variations in nanoscale surface energy and the lattice interaction with the substrate. This may also explain differences in required annealing time found for sapphire substrates of different orientations (c-cut and r-cut) as described above.

3. CONCLUSION

In summary, we have developed a high-vacuum gas evolution technique that allows for the precise modification of oxygen stoichiometry in VO_x thin films. Using temperature-dependent electrical transport measurements, x-ray diffraction and reciprocal space mapping, we show that optimal oxygen stoichiometry is obtained in each of the transformed films. Based on our technique, the thermodynamic phase diagram can be well-defined and elucidated for the V-O system when scaling down the VO_x from bulk into thin film form. Our results may play an important role in improving and controlling transport properties across the MIT in oxide-based devices. It may open a new way to synthesize exotic or Magnéli phase oxide films which cannot be directly grown by standard deposition techniques. We hope our work will encourage the use of gas evolution methods in other complex oxide systems.

ACKNOWLEDGMENTS

The authors acknowledge support from the Air Force Office of Scientific Research grant FA9550-14-1-0202, supported by the Vannevar Bush Faculty Fellowship program, sponsored by the Basic Research Office of the Assistant Secretary of Defense for Research and Engineering and funded by the Office of Naval Research through grant N00014-15-1-2848. J.d.V. thanks Fundación Ramón Areces for their funding.

4. EXPERIMENTAL

Thin-film growth

Single-phase VO₂ and V₂O₃ thin films were deposited on 7×12 mm² (012) r-cut or (001) c-cut sapphire (α-Al₂O₃) substrates using RF magnetron sputtering from a V₂O₃ target. As described in previous studies^[9,39], the growth of VO₂ was done at a substrate temperature of 520 °C in an environment of Ar/O₂ mixture (8% O₂) at 3.7 mTorr. The V₂O₃ thin films were prepared at a 700 °C substrate temperature in an environment of ultrahigh purity Ar (>99.999%) at 8 mTorr.

Gas evolution system

A high-vacuum oxygen annealing method was developed to synthesize complex oxide thin films with controlled oxygen stoichiometry. The experimental setup is shown in Fig. 1a. The base pressure in the system is $\sim 1 \times 10^{-7}$ torr. Thin film samples were placed into the center of a Lindberg/Blue MTM 1200°C tube furnace for heat treatment under different oxygen atmospheres. The PO₂ was measured using a Residual Gas Analyzer equipped with a quadrupole mass spectrometer (UHV to 10⁻⁴ torr) and two capacitance manometers (10⁻⁴ torr to 1000 torr). A MKS Series 245 pressure/flow control valve, a variable leak valve and a solenoid valve were used to carefully control the PO₂. High purity oxygen (>99.99%) was introduced into the annealing chamber using the computer-controlled metal-seated valve. This gas evolution setup provides a wide pressure range (UHV to 1000 torr) and allows for the continuous variation of the PO₂ under high vacuum conditions.

Evolution of V₂O₃ phase into VO₂

Oxidation of as-deposited V₂O₃/Al₂O₃ (r-cut) thin films with 75 nm thickness was performed in the gas evolution system by continuously controlling PO₂ and T. The annealing conditions were chosen according to the known bulk vanadium-oxygen phase diagram.^[24-26] By carefully following thermodynamically stable paths, different oxidation states of vanadium could be obtained from V₂O₃. At the start of route I (A→B→C→B→A) (see Fig. 1b), PO₂ was fixed to 1×10^{-6} torr and the temperature was ramped up to 500 °C at a heating rate of 10 °C/min. After reaching 500 °C, the PO₂ was continuously increased along (B→C) in order to keep the sample in the potentially stable region of the VO₂ phase in PO₂-T diagram. The sample was then annealed at 600 °C for three hours with PO₂ $\sim 7 \times 10^{-4}$ torr (at point C in Fig. 1b). After reaching thermodynamic equilibrium, both PO₂ and T were reduced at a cooling rate of 6 °C/min along the return path (C→B). After reaching 500 °C, the sample was then quenched to room temperature by transferring it to the load lock.

Similarly, by following route II (A→B→C→D), the oxygen stoichiometry in as-deposited V₂O₃ can be modified, leading to a transformation into a higher oxidation state. After a three-hour reaction at 600 °C (point C), the sample was cooled down to room temperature under continuous oxygen flow at PO₂ $\sim 7 \times 10^{-4}$ torr. As will be discussed later, this method

produces high-quality VO₂ thin films with sharp metal-insulator transitions. The ability to continuously and gradually control both PO₂ and T is important for maintaining thermodynamic equilibrium in the thin film sample at all times so as to prevent the formation of possible secondary phases during the process.

Evolution of V₂O₃ phase into V₃O₅

For the oxidation reaction of V₂O₃ into V₃O₅, we used a similar procedure. At the start of route III (E→H→I), an as-deposited V₂O₃/Al₂O₃ (c-cut) film with thickness of approximately 100 nm was mounted in the tube furnace and the PO₂ was fixed to $\sim 4 \times 10^{-9}$ torr. The temperature was then increased from RT to 800 °C at a rate of 10 °C/min (E→H). From point H, both the PO₂ and temperature (T) were continuously increased along the possible stable region for V₃O₅. The thin film was then annealed for three hours at 838 °C with PO₂ $\sim 8 \times 10^{-8}$ torr (at point I). After reaching phase equilibrium, both PO₂ and T were continuously reduced along the return route (I→H) at a cooling rate of 6 °C/min and the sample was quenched from 800 °C to room temperature along the return path (H→E). For the case of V₂O₃/Al₂O₃ (r-cut) film, we performed the same experiment: the 100 nm film was annealed following route III. The annealing time was 3 hours at point I in the first round and increased to 6 hours for the second round.

Evolution of VO₂ phase into V₂O₃

In order to understand the phase stability of VO₂, as-deposited VO₂/Al₂O₃ (r-cut) films with thickness of 75 nm were heat-treated under two different thermodynamic paths: route IV (E→F→E) and route V (E→G→E). At the start of route IV, the temperature was increased at a rate of 10 °C/min to 550 °C under PO₂ $\sim 4 \times 10^{-9}$ torr. The annealing time was optimized to 12 hours. After the reduction reaction, the sample was then rapidly quenched in order to prevent the formation of other Magnéli phases that might occur during a slow cooling process. Similarly, along thermodynamic route V, the sample was stabilized at 838 °C for 12 hr (point G) and also rapidly quenched to room temperature.

Characterizations

Room-temperature θ -2 θ x-ray diffraction (XRD) and reciprocal space mapping (RSM) were used to characterize the lattice structure and its relation to the substrate structure using a Rigaku SmartLab x-ray diffractometer with Cu K α radiation ($\lambda = 1.54$ Å). Atomic force microscopy (AFM) for room-temperature surface characterization was performed using a Veeco Scanning Probe Microscope (SPM). The scan area of each of the films was fixed to $1 \times 1 \mu\text{m}^2$. Temperature-dependent electrical transport measurements using a standard four-point probe configuration were performed in a Lakeshore TTPX probe station with a Keithley 6221 current source and a Keithley 2182A nanovoltmeter.

REFERENCES

- [1] M. Imada, A. Fujimori, Y. Tokura, *Rev. Mod. Phys.* **70**, 1039 (1998).
- [2] J. H. Ngai, F. J. Walker, C. H. Ahn, *Annu. Rev. Mater. Res.* **44**, 1 (2014).
- [3] Z. Yang, C. Ko, S. Ramanathan, *Annu. Rev. Mater. Res.* **41**, 337 (2011).
- [4] D. Lee, J. Lee, K. Song, F. Xue, S.-Y. Choi, Y. Ma, J. Podkaminer, D. Liu, S.-C. Liu, B. Chung, W. Fan, W. Zhou, J. Lee, L.-Q. Chen, S. H. Oh, Z. Ma, C. B. Eom, *Nano Lett.* **17**, 5614 (2017).
- [5] F. J. Morin, *Phys. Rev. Lett.* **3**, 34 (1959).
- [6] J. Jeong, N. Aetukuri, T. Graf, T. D. Schladt, M. G. Samant, S. S. P. Parkin, *Science* **339**, 1402 (2013).
- [7] J. Cao, Y. Gu, W. Fan, L. Q. Chen, D. F. Ogletree, K. Chen, N. Tamura, M. Kunz, C. Barrett, J. Seidel, J. Wu, *Nano Lett.* **10**, 2667 (2010).
- [8] A. Cavalleri, Th. Dekorsy, H. H. W. Chong, J. C. Kieffer, R. W. Schoenlein, *Phys. Rev. B* **70**, 161102 (2004).
- [9] J. del Valle, Y. Kalcheim, J. Trastoy, A. Charnukha, D. N. Basov, I. K. Schuller, *Phys. Rev. Appl.* **8**, 054041 (2017).
- [10] Y. Zhou, S. Ramanathan, *Proc. IEEE* **103**, 1289 (2015).
- [11] J. del Valle, P. Salev, F. Tesler, N. M. Vargas, Y. Kalcheim, P. Wang, J. Trastoy, M.-H. Lee, G. Kassabian, J. G. Ramírez, M. J. Rozenberg, I. K. Schuller, *Nature* **569**, 388 (2019).
- [12] J. del Valle, J. G. Ramírez, M. J. Rozenberg, I. K. Schuller, *J. Appl. Phys.* **124**, 211101 (2018).
- [13] K. Held, G. Keller, V. Eyert, D. Vollhardt, V. I. Anisimov, *Phys. Rev. Lett.* **86**, 5345 (2001).
- [14] D. B. McWhan, T. M. Rice, J. P. Remeika, *Phys. Rev. Lett.* **23**, 1384 (1969).
- [15] J. G. Ramirez, T. Saerbeck, S. Wang, J. Trastoy, M. Malnou, J. Lesueur, J.-P. Crocombette, J. E. Villegas, I. K. Schuller, *Phys. Rev. B* **91**, 205123 (2015).
- [16] Y. Kalcheim, N. Butakov, N. M. Vargas, M.-H. Lee, J. del Valle, J. trastoy, P. Salev, J. Schuller, I. K. Schuller, *Phys. Rev. Lett.* **122**, 057601 (2019).
- [17] R. Jaramillo, F. Schoofs, S. D. Ha, S. Ramanathan, *J. Mater. Chem. C* **1**, 2455 (2013).
- [18] N. Kumar, A. Rúa, J. Lu, F. Fernández, S. Lysenko, *Phys. Rev. Lett.* **119**, 057602 (2017).
- [19] B. Fisher, L. Patlagan, K. B. Chashka, C. Makarov, G. M. Reisner, *Appl. Phys. Lett.* **109**, 103501 (2016).

- [20] D. Lee, J. Park, J. Park, J. Woo, E. Cha, S. Lee, K. Moon, J. Song, Y. Koo, H. Hwang, *Adv. Mater.* **27**, 59 (2015).
- [21] U. Schwingenschlögl, V. Eyert, *Ann. Phys.* **13**, 475 (2004).
- [22] K. Kosuge, *J. Phys. Chem. Solids* **28**, 1613 (1967).
- [23] C. H. Griffiths, H. K. Eastwood, *J. Appl. Phys.* **45**, 2201 (1974).
- [24] Y. B. Kang, *J. Eur. Ceram. Soc.* **32**, 3187 (2012).
- [25] J. Haber, M. Witko, R. Tokarz, *Appl. Catal., A* **157**, 3 (1997).
- [26] W. Brückner, H. Oppermann, W. Reichelt, E.I. Terukov, F.A. Tschudnowski, E. Wolf, *Vanadiumoxide*, Akademie-Verlag, Berlin (1983)
- [27] K. Liu, S. Lee, S. Yang, O. Delaire, J. Wu, *Mater. Today* **21**, 875 (2018)
- [28] A. Navrotsky, C. Ma, K. Lilova, N. Birkner, *Science* **330**, 199 (2010).
- [29] A. Navrotsky, *ChemPhysChem* **12**, 2207 (2011).
- [30] X. Liu, S.-W. Wang, F. Chen, L. Yu, X. Chen, *J. Phys. D: Appl. Phys.* **48**, 265104 (2015).
- [31] Y.-K. Dou, J.-B. Li, M.-S. Cao, D.-Z. Su, F. Rehman, J.-S. Zhang, H.-B. Jin, *Appl. Surf. Sci.* **345**, 232 (2015)
- [32] B. V. Bilzen, P. Homm, L. Dillemans, C.-Y. Su, M. Menghini, M. Sousa, C. Marchiori, L. Zhang, J. W. Seo, J.-P. Locquet, *Thin Solid Films* **591**, 143 (2015)
- [33] F. A. Chudnovskii, E. I. Terukov and D. I. Khomskii, *Solid State Commun.* **25**, 573 (1978).
- [34] E. I. Terukov, F. A. Chudnovskii, W. Reichelt, H. Oppermann, W. Brückner, H.-P. Brückner, W. Moldenhauer, *Phys. Stat. Sol. A* **37**, 541 (1976)
- [35] A. Rúa, R. D. Díaz, N. Kumar, S. Lysenko, F. E. Fernández, *J. Appl. Phys.* **121**, 235302 (2017).
- [36] E. Osquiguil, M. Maenhoudt, B. Wuyts, and Y. Bruynseraede, *Appl. Phys. Lett.* **60**, 1627 (1992).
- [37] J. Hasen, D. Lederman, I. K. Schuller, V. Kudinov, M. Maenhoudt, Y. Bruynseraede, *Phys. Rev. B* **51**, 1342 (1995).
- [38] G. Rampelberg, B. De Schutter, W. Devulder, K. Martens, I. Radu, C. Detavernier, *J. Mater. Chem. C* **3**, 11357 (2015).
- [39] J. Trastoy, Y. Kalcheim, J. del Valle, I. Valmianski, I. K. Schuller, *J. Mater. Sci.* **53**, 9131 (2018).
- [40] S. J. Pennycook, H. Zhou, M. F. Chisholm, A. Y. Borisevich, M. Varela, J. Gazquez, T. J. Pennycook, J. Narayan, *Acta Mater.* **61**, 2725 (2013).
- [41] H. Katzke, P. Tolédano, W. Depmeier, *Phys. Rev. B* **68**, 024109 (2003).

- [42] R. Molaei, R. Bayati, F. Wu, J. Narayan, *J. Appl. Phys.* **115**, 164311 (2014)
- [43] J. Narayan, V. M. Bhosle, *J. Appl. Phys.* **100**, 103524 (2006).
- [44] D. Brassard, S. Fourmaux, M. Jean-Jacques, J. C. Kieffer, M. A. El Khakani, *Appl. Phys. Lett.* **87**, 051910 (2005).
- [45] S. Zhang, I. S. Kim, L. J. Lauhon, *Nano Lett.* **11**, 1443 (2011).
- [46] Z. Zhang, F. Zuo, C. Wan, A. Dutta, J. Kim, J. Rensberg, R. Nawrodt, H. H. Park, T. J. Larrabee, X. Guan, Y. Zhou, S. M. Prokes, C. Ronning, V. M. Shalaev, A. Boltasseva, M. A. Kats, S. Ramanathan, *Phys. Rev. Applied* **7**, 034008 (2017).
- [47] J. Sakai, P. Limelette, H. Funakubo, *Appl. Phys. Lett.* **107**, 241901 (2015).
- [48] J. Brockman, M. G. Samant, K. P. Roche, S. S. P. Parkin, *Appl. Phys. Lett.* **101**, 051606 (2012).
- [49] V. N. Andreev, V. A. Klimov, *Phys. Solid State* **53**, 2424 (2011).
- [50] Powder Diffraction File 72-0977, International Centre for Diffraction Data, PA, USA.
- [51] V.A. Sidorov, A Waskowska, D. Badurski, *Solid State Commun.* **125**, 359 (2003).
- [52] J. Brockman, N. P. Aetukuri, T. Topuria, M. G. Samant, K. P. Roche, S. S. P. Parkin, *Appl. Phys. Lett.* **98**, 152105 (2011).
- [53] S. A. Shivashankar, J. M. Honig, *Phys. Rev. B* **28**, 5695 (1983).
- [54] Y. Ueda, K. Kosuge, S. Kachi, *J. Solid State Chem.* **31**, 171 (1980).